PAPER

Check for updates

Thermal and bisphenol-A adsorption properties of a zinc ferrite/β-cyclodextrin polymer nanocomposite†

Ruksana Sirach and Pragnesh N. Dave *

The present study investigated the use of a nanocomposite, produced by reinforcing nanosize zinc ferrite (ZnFe$_2$O$_4$) in a porous β-CD based polymeric matrix (β-CD-E-T/ZnFe$_2$O$_4$), for the removal of Bisphenol A (BPA) from aqueous solutions *via* adsorption. The thermal stability of the β-CD-based polymer and β-CD-E-T/ZnFe$_2$O$_4$ nanocomposite were investigated using simultaneous thermal analysis at four heating rates. Non-isothermal isoconversion methods were employed to study the thermal degradation kinetics of the β-CD based polymer before and after ZnFe$_2$O$_4$ nano-filling. The results showed that ZnFe$_2$O$_4$ nano-reinforcement increased the activation energy barrier for the thermal degradation of the β-CD-based polymeric matrix. Adsorption experiments showed that the β-CD-E-T/ZnFe$_2$O$_4$ nanocomposite exhibited very high BPA adsorption within 5 minutes. Isotherm, kinetics, and thermodynamic investigations revealed that the adsorption of BPA was *via* multilayer adsorption on a heterogeneous β-CD-E-T/ZnFe$_2$O$_4$ surface. The thermodynamic studies indicated that BPA adsorption on β-CD-E-T/ZnFe$_2$O$_4$ was spontaneous and exothermic. Overall, the β-CD-E-T/ZnFe$_2$O$_4$ nanocomposite showed less thermal degradation and high efficiency for removing BPA from contaminated water, indicating its potential as a promising material for wastewater treatment applications.

1. Introduction

Bisphenol A (2,2-bis(4-hydroxyphenyl)propane; BPA) is a diphenylmethane derivative. BPA is known to exhibit toxic properties and can disrupt the normal function of endogenous hormones. Studies have shown that BPA exposure can lead to an increased risk of cancer and other adverse health effects.[1–3] Polycarbonate plastic is commonly utilized in the packaging of food, beverages, medical equipment, dental supplies, and thermal paper. However, due to the susceptibility of plastic materials to release BPA under certain conditions such as high temperatures, and basic or acidic environments, these plastic products may contaminate food and beverages with BPA. A survey conducted by National Health and Nutrition Examination Survey (NHANES; United States; 2013–2014) revealed that BPA was detected in 95.7% of randomly selected urine samples. The median concentration of BPA in urine samples from adults and children in the United States was found to be 1.24 μg L^{-1} and 1.25 μg L^{-1}, respectively. Notably, the concentration of BPA in these samples was significantly higher than its other derivatives, such as bisphenol F and bisphenol S.[4] Analysis of samples collected by Fürhacker *et al.*[5] from various wastewater sources,

including metal/wood manufacturing, chemical industry, hospitals, paper production, cloth washing companies, household areas, and food industry, revealed that the concentration of BPA varied widely, ranging from 1 to 72 μg L^{-1}. Notably, the highest concentration of BPA was found in samples collected from paper production sites. The harmful effects of BPA have prompted the development of efficient technologies for its removal from wastewater. Advanced oxidation, biodegradation, photocatalytic degradation, membrane filtration, and adsorption processes are among the methods that have been reported for the treatment of BPA. These techniques are often employed in combination to achieve more efficient removal of BPA. Further research is needed to identify the most effective and sustainable approach for the removal of BPA from different sources.[6–12] Adsorption is a simple, cost-effective, and fast method for the removal of BPA from wastewater. The effectiveness of this process can be further improved by tailoring the functionality of the adsorbent material. Conventional adsorbent materials, such as activated carbons and clay, may have slower adsorption rates and limited tailoring properties, making it challenging to achieve optimal results. For instance, Martín-Lara *et al.*[13] reported that it took activated carbon 2880 minutes to reach equilibrium during the removal of BPA. Another study demonstrated that activated carbons derived from biomass can exhibit a high adsorption capacity (>458 mg g^{-1}) for both anionic and cationic adsorbates, as determined by Langmuir adsorption isotherm.[14] Similarly, other studies

Department of Chemistry, Sardar Patel University, Vallabh Vidyanagar, 388 120, Gujarat, India. E-mail: pragnesh7@yahoo.com

† Electronic supplementary information (ESI) available. See DOI: https://doi.org/10.1039/d3ra03331g

investigating the use of activated carbon as a sorbent have also noted a lack of selectivity.[15,16] Additionally, natural clays rich in smectite, when used as adsorbents, did not exhibit significant changes in selectivity between anionic and cationic adsorbates.[17] Pleșa Chicinaș et al.[18] utilized bentonite clay to remove cationic and anionic dyes, wherein the clay displayed a slightly higher adsorption capacity for the cationic dye compared to the anionic dye, albeit with a negligible difference (<15 mg g^{-1}). Other potential adsorbent materials, such as metal–organic frameworks (MOFs), have also been explored.[19–21] Although MOFs can demonstrate good adsorption performance, their stability is compromised under certain conditions, such as exposure to water or acidic/alkaline environments.[22] Therefore, it is necessary to utilize adsorbent materials whose properties can be tailored according to the specific adsorbate being targeted for removal. By employing such tailored adsorbents, the efficacy of the adsorption process can be enhanced, leading to a more efficient BPA removal method.

Polysaccharides represent a substantial class of naturally occurring biological macromolecules, consisting of repeating units of monosaccharides, such as glucose and fructose. Due to their abundance, biodegradable nature, nontoxic properties, and cost-effectiveness, polysaccharides have gained significant attention for a broad range of applications. As a result, they have emerged as one of the most promising and versatile materials for various scientific and industrial applications.[23] Starch is a widely available polysaccharide found naturally in sources such as potatoes, rice, wheat, sweet potatoes, and corn. One of the intriguing chemical compounds obtained from starch is cyclodextrins, which are oligosaccharides composed of 3 to 10 monosaccharides in their structure. Cyclodextrins and their derivatives are formed from glucopyranose units linked together through glycosidic bonds to form ring structures. These structures are further classified into α, β, and γ-cyclodextrins, consisting of 6, 8, and 10 glucopyranose units, respectively. β-Cyclodextrin (β-CD), composed of eight glucopyranose units, has a cone-shaped structure with an inner hydrophobic cavity (0.60–0.65 nm) and an outer hydrophilic portion, owing to the abundance of hydroxyl (–OH) groups.[24] β-CD is a promising material for various scientific and industrial applications due to its unique shape and chemical properties. One of the distinctive properties of β-CD is its ability to host or trap various organic molecules within its cavity, β-CD, and its derivatives have been extensively investigated as potential drug delivery carriers, owing to their host–guest interaction properties. The host–guest interaction of β-CD with organic molecules makes it a promising material for wastewater treatment. However, the direct use of β-CD in wastewater treatment may not be efficient due to its partial solubility in water (18.6 mg mL^{-1}) and the potential for creating secondary pollutants during its application.[25] To address the issue, various β-CD based polymers and their nanocomposites are being extensively researched for the potential removal of BPA from the wastewater. Despite these efforts, effective removal of BPA remains a significant challenge, as β-CD based materials exhibit low adsorption capacity, slow adsorption rates, poor removal efficiency, and challenging regeneration processes.[26–30] Previous studies have reported on the successful use of β-CD-based porous polymers, such as β-CD-epichlorohydrin (ECH; E)-tetrafluoroterephthalonitrile (TFTPN; T) and β-CD-4,4′-bis(chloromethyl) biphenyl, which contain aromatic moieties, for the rapid removal of BPA from aqueous solutions with high adsorption capacity.[26,28] However, these polymers exhibited low equilibrium adsorption capacity, which limits their practical application. Thus, there is a need for further improvement in the design and synthesis of β-CD-based polymers to enhance their adsorption capacity and efficiency for the removal of BPA from wastewater.

The incorporation of nanosize (size < 100 nm) reinforcement materials is a common approach to enhance the adsorption capacity of polymers used in wastewater treatment.[31–34] Among the widely used reinforcements for polymers: clays, metal oxides, and carbon-based nanomaterials have gained significant attention. Metal oxides such as zinc oxide (ZnO) and magnetite (Fe$_3$O$_4$) have been extensively studied for improving the adsorption performance of polymers. However, the selection of reinforcement materials for composite production should be based on their synergetic effect to improve the removal of BPA. For instance, previously reported composites, such as β-CD-capped graphene–magnetite nanocomposite and carboxymethyl-β-CD polymer/Fe$_3$O$_4$, exhibited a slow adsorption rate for BPA.[27,29] Ferrites (MFe$_2$O$_4$; where M represents metal ions in a 2+ state) have been utilized in a variety of applications, including catalysis and semiconductor technology. Zinc ferrite (ZnFe$_2$O$_4$) has previously been employed to enhance the adsorption performance of polymeric films due to its high specific surface area and the synergistic effects between Fe and Zn.[35] ZnFe$_2$O$_4$ can be synthesized using methods such as the co-precipitation, hydrothermal, sol–gel, and thermal decomposition to name a few. The hydrothermal method can provide better nanosized ZnFe$_2$O$_4$ particles with narrow particle size distributions. Therefore, the authors opted for the modified hydrothermal method to synthesize nanoscale ZnFe$_2$O$_4$.

The present study investigates the use of a nanocomposite, β-CD-E-T/ZnFe$_2$O$_4$ reported in our previous work[36] for the removal of BPA from an aqueous solution. The thermal stability and degradation of the nanocomposite were examined at various heating rates (5, 10, 15, and 20 °C min^{-1}) to evaluate the influence of ZnFe$_2$O$_4$ reinforcement. The adsorption of BPA onto β-CD-E-T/ZnFe$_2$O$_4$ was studied under different conditions, and the isotherm, kinetic, and thermodynamic properties of the adsorption process were investigated to determine its efficiency. Furthermore, the Fourier transform infrared spectroscopy (FTIR) spectra of the nanocomposite were obtained both before and after the adsorption process to evaluate potential interactions responsible for the adsorption of BPA. It should be noted that, to the best of the author's knowledge, the utilization of the β-CD-E-T/ZnFe$_2$O$_4$ nanocomposite for the removal of BPA has not been reported thus far.

2. Experimental

2.1. Synthesis of β-CD-E-T/ZnFe$_2$O$_4$ nanocomposite

All the chemicals used in this study were received from their respective suppliers (Table S1†) and used as received without additional modifications.

For the synthesis of β-CD-E-T polymer, the previously reported method was adopted with a few modifications.[26] In our previous work,[36] a detailed description of the synthesis procedure was provided. Briefly, 25 g of β-CD was dissolved in 37.5 mL of 6 N NaOH at 80 °C with vigorous stirring. Then, 3.75 g of TFTPN was added to the basic β-CD solution, and the resulting solution was stirred for 60 minutes before being irradiated with ultrasound in an ultrasound bath for 10 minutes. Afterward, the solution was stirred again, and 31.3 mL of ECH was slowly injected into the solution. Gelation was observed after 13 minutes of the complete addition of ECH. The obtained gel was washed with water several times to remove the soluble polymer fraction and then washed with acetone (Soxhlet) for 8 hours to remove impurities.

To synthesize $ZnFe_2O_4$, $Zn(NO_3)_2 \cdot 6H_2O$ and $Fe(NO_3)_3 \cdot 9H_2O$ were mixed in 100 mL of ethylene glycol in a 1 : 2 mole ratio. Later, sodium acetate (Fe^{3+} : sodium acetate mole ratio = 1 : 4) was added. The mixture was vigorously stirred for 60 minutes and then subjected to ultrasound irradiation for 20 minutes. Next, 25 mL of ethylene diamine was added to the solution, and the resulting mixture was again irradiated with ultrasound for 20 minutes. After stirring the solution for 60 minutes, it was kept in an oven at 180 °C for 3 days until precipitations of $ZnFe_2O_4$ were obtained. The insoluble content was filtered and washed with water to remove any unreacted impurities and then dried in an oven at 60 °C. Finally, the material was calcined at 500 °C for 3 hours.

To synthesize the β-CD-E-T/$ZnFe_2O_4$ nanocomposite, an appropriate amount of β-CD-E-T polymer (90% by mass) was dissolved in a mixture of tetrahydrofuran and water (2 : 1 ratio). The solution was stirred at 60 °C until the β-CD-E-T was completely dissolved. Thereafter, $ZnFe_2O_4$ (10% by mass) was added to β-CD-E-T solution and subjected to ultrasound irradiation for 20 minutes, followed by stirring for 2 hours. Finally, the solvents were evaporated in an oven to obtain the β-CD-E-T/$ZnFe_2O_4$ nanocomposite.

2.2. Characterization

FTIR spectroscopy was used to study structural changes in β-CD-E-T/$ZnFe_2O_4$ to confirm the formation of interaction between BPA and β-CD-E-T/$ZnFe_2O_4$. FTIR analysis was carried out between 400–4000 cm^{-1} wavenumber range (PerkinElmer, USA) using transmittance mode against KBr reference. For FTIR measurement, the samples were pre-heated in an oven to eliminate moisture. Specifically, 1 mg of the sample was thoroughly mixed with 190 mg of KBr using a mortar and pestle, resulting in a fine powder. Subsequently, the powder was compressed into pellets using a manual hydraulic press. Nova Nano FE-SEM 450 (FEI) was used to confirm the nanosize of $ZnFe_2O_4$ and reinforcement of $ZnFe_2O_4$ in the β-CD-E-T polymer matrix. Nova Touch LX2; Quantachrome Instruments was used to calculate the pore size, pore volume, and surface area of β-CD-E-T/$ZnFe_2O_4$. The sample was degassed at 150 °C for 5 hours before N_2 physisorption analysis. To study the effect of $ZnFe_2O_4$ reinforcement on the thermal stability of β-CD-E-T polymer, the TG-DTG curves of the sample were obtained using 5000/2960

STA; TA instruments under 150 mL min^{-1} N_2 gas flow between 30–600 °C in an alumina pan at 5, 10, 15, and 20 °C min^{-1} heating rates.

2.3. Adsorption and regeneration studies

The concentration of BPA before and after adsorption was monitored using SHIMADZU TCC-240 A UV-vis spectrophotometer taking water as a reference solvent. The calibration curve of BPA was generated by plotting the absorbance of BPA at λ_{max} = 276 nm against concentration (3–30 mg L^{-1}) (Fig. S1†). The before and after adsorption concentration of BPA was used to calculate the removal efficiency ($R\%$; eqn (1)) and adsorption capacity (q_e; eqn (2)) of β-CD-E-T/$ZnFe_2O_4$.

$$R\% = \frac{C_0 - C_e}{C_0} \times 100\% \tag{1}$$

$$q_e = (C_0 - C_e) \times \frac{V}{m} \tag{2}$$

where C_0, C_e, V, and m represent initial BPA concentration (mg L^{-1}), final BPA concentration (mg L^{-1}), the volume of BPA solution (L), and mass of β-CD-E-T/$ZnFe_2O_4$ adsorbent (g), respectively.

Adsorption isotherms can provide information on the nature of the adsorption process (*i.e.*, physical, or chemical adsorption), as well as the types of interactions that occur between the BPA and β-CD-E-T/$ZnFe_2O_4$ adsorbent. There are a total of four Langmuir linear equations given in the ESI File (eqn (S1)–(S4)).† Adsorption models like Freundlich (eqn (3)), Tempkin (eqn (4)), Langmuir (eqn (5)), and Dubinin–Radushkevich (eqn (6)) were tested to obtain isotherm parameters of adsorption of BPA on β-CD-E-T/$ZnFe_2O_4$. Moreover, the separation factor (R_L), Polanyi potential (ε), and energy (E) of the adsorption were calculated using eqn (7), (8), and (9), respectively.

$$\log q_e = \log K_F + \frac{1}{n}\log C_e \tag{3}$$

$$q_e = B_1 \ln A_T + B_1 \ln C_e \tag{4}$$

$$\frac{1}{q_e} = \frac{1}{q_m} + \frac{1}{q_m K_L} \times \frac{1}{C_e} \tag{5}$$

$$\ln q_e = \ln q_m - \delta \varepsilon^2 \tag{6}$$

$$R_L = \frac{1}{1 + K_L C_0} \tag{7}$$

$$\varepsilon = RT \ln\left(\frac{C_s}{C_e}\right) \tag{8}$$

$$E = \frac{1}{\sqrt{2\delta}} \tag{9}$$

In this context, the symbols R, T, q_m, K_L, K_F, n, b_T, A_T, δ, and C_s are employed to respectively denote the universal gas constant (8.314 J mol^{-1} K^{-1}), the temperature during adsorption, Langmuir maximum adsorption capacity (mg g^{-1}), Langmuir constant, Freundlich constant, heterogeneity factor, Temkin

constant, Temkin equilibrium binding constant ($L\ g^{-1}$), constant related to the energy of the adsorption (eqn (9)), and saturation concentration of BPA. The value of b_T was calculated using the relation $B_1 = RT/b_T$.

To describe the kinetics of BPA adsorption on β-CD-E-T/ZnFe$_2$O$_4$, we employed four different models: pseudo-second-order (eqn (10)), pseudo-first-order (eqn (11)), Elovich (eqn (12)), and intraparticle diffusion (eqn (13)). We then determined the best fitting model based on the experimental data to get information about the kinetics of the adsorption of BPA on β-CD-E-T/ZnFe$_2$O$_4$.

$$\frac{t}{q_t} = \frac{1}{K_2\,q_e^2} + \frac{t}{q_e} \qquad (10)$$

$$\log(q_e - q_t) = \log q_e - \frac{k_1 t}{2.303} \qquad (11)$$

$$q_t = \frac{\ln a_e b_e}{b_e} + \frac{1}{b_e}\ln t \qquad (12)$$

$$q_t = k_p t^{0.5} + C \qquad (13)$$

where q_t, k_p, t, k_1, k_2, and a_e; b_e represents adsorption capacity at 't' time (min), intraparticle diffusion constant, time (min), pseudo-first-order constant, pseudo second order constant, and Elovich constants, respectively. The width of the boundary layer and its impact on the rate of adsorption can be elucidated using the variable 'C'.

Moreover, the effect of temperature was used to investigate the nature of the adsorption of BPA on β-CD-E-T/ZnFe$_2$O$_4$. The slope and interception of the plot of $\ln k_e$ against $1000/T$ (K^{-1}) were used to calculate thermodynamic parameters like enthalpy change ($\Delta H°$) and entropy change ($\Delta S°$) using eqn (14). The value of $\Delta H°$ and $\Delta S°$ was used to calculate free energy change ($\Delta G°$) using eqn (15).

$$\ln k_e = \frac{\Delta S°}{R} - \frac{\Delta H°}{RT} \qquad (14)$$

$$\Delta G° = \Delta H° - T\Delta S° \qquad (15)$$

where $k_e = q_e/C_e$.

To regenerate the adsorbent, the spent adsorbent, BPA-loaded β-CD-E-T/ZnFe$_2$O$_4$, was washed with acetone under continuous stirring and dried in an oven at 60 °C. The regenerated β-CD-E-T/ZnFe$_2$O$_4$ was reused for up to five cycles to evaluate the adsorption reusability of the nanocomposites.

3. Results and discussions

3.1. Structural and surface characteristics

FTIR spectrum of β-CD-E-T and β-CD-E-T/ZnFe$_2$O$_4$ is given in Fig. 1. In the FTIR spectrum, a broad peak between 3000–3700 cm^{-1} was observed because of the large number of the hydroxyl group present in the β-CD moiety giving rise to O–H stretching vibrations. The peak between 3000–2800 cm^{-1} was observed because of C–H stretching vibrations. The peak at

~2381–2291 cm^{-1} confirmed the presence of the nitrile group in the TFTPN moiety, thereby indicating the presence of the TFTPN fragment in the synthesized β-CD-E-T/ZnFe$_2$O$_4$ nanocomposite. The characteristic band at 1700–1550 cm^{-1} corresponds to carbohydrates (from β-CD) present in the β-CD-E-T polymer matrix. O–H and C–H bending vibrations, C–O, C–O–C, and aromatic C–C stretching vibrations give rise to peaks between 1530–1230 cm^{-1}. Additionally, peaks corresponding to C–O–C at 1087 cm^{-1} and C–O/C–C stretching vibrations at 1041 cm^{-1} were observed in the FTIR spectrum of β-CD-E-T/ZnFe$_2$O$_4$. Peaks below 1000 cm^{-1} were complex and could not be accurately assigned, but were thought to arise from various bending vibrations in the glucopyranose moiety (from β-CD) and ZnFe$_2$O$_4$.[36,37]

To investigate potential interactions between β-CD-E-T/ZnFe$_2$O$_4$ and BPA, the FTIR spectra of β-CD-E-T/ZnFe$_2$O$_4$ and β-CD-E-T/ZnFe$_2$O$_4$ loaded with BPA (Fig. 1b) were analyzed. The FTIR spectrum of BPA exhibited bands that were consistent with prior findings in the literature.[38] There were no major changes in the FTIR spectrum of β-CD-E-T/ZnFe$_2$O$_4$ before and after BPA adsorption. Most peaks in β-CD-E-T/ZnFe$_2$O$_4$ maintained the same position and width before and after BPA adsorption. However, the –O–H stretching vibration band between 3700–3000 cm^{-1} in β-CD-E-T/ZnFe$_2$O$_4$ was broadened after BPA adsorption. A similar peak broadening for the –OH group (3700–3000 cm^{-1}) was observed in BPA-adsorbed covalent organic frameworks.[19] According to previous publications, –OH was crucial in the formation of hydrogen bonds between adsorbent and BPA, which promoted the adsorption of organic pollutants.[19,39,40] This suggested that –OH probably had
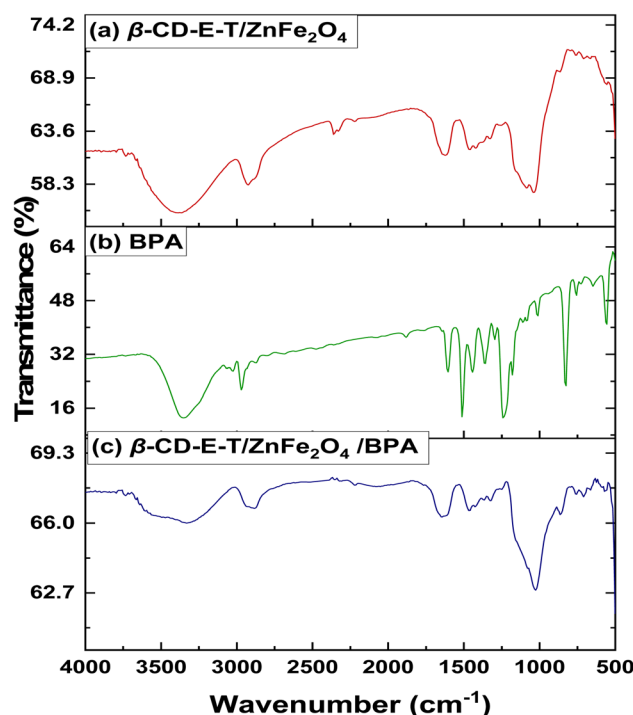

Fig. 1 FTIR spectrum of (a) β-CD-E-T/ZnFe$_2$O$_4$, (b) BPA, and (c) β-CD-E-T/ZnFe$_2$O$_4$ after BPA adsorption.

a significant impact on the adsorption procedure. Therefore, hydrogen bonding may have played a significant role in the adsorption of BPA onto β-CD-E-T/ZnFe$_2$O$_4$. The peak corresponding to nitrile stretching vibration ($\sim$2381–2291 cm^{-1}) was eliminated in BPA-loaded β-CD-E-T/ZnFe$_2$O$_4$, indicating a strong interaction between BPA and β-CD-E-T/ZnFe$_2$O$_4$ nanocomposite. Moreover, BPA is a diphenylmethane derivative with a π–electron cloud. This allows the π–π interactions between BPA and TFTPN moiety from β-CD-E-T/ZnFe$_2$O$_4$ nanocomposite. Additionally, the hydroxyl groups in BPA make the electron-rich and polar areas more prominent, resulting in enhanced π–π interaction between BPA and β-CD-E-T/ZnFe$_2$O$_4$.[40] The observed π–π interaction could have been responsible for the reduction in the peak within the range of $\sim$2381–2291 cm^{-1}. Additionally, the peaks at 1087 and 1041 cm^{-1} in β-CD-E-T/ZnFe$_2$O$_4$ shifted to lower wavenumber values (*i.e.*, 1080 and 1034 cm^{-1}) suggesting possible interactions between BPA and glucopyranose fragment (C–O–C/C–O) of β-CD. However, the hydrophobic/host guest interactions between β-CD from β-CD-E-T/ZnFe$_2$O$_4$ and BPA is also possible.[41,42]

β-CD-E-T polymer (Fig. 2a) exhibited an irregular morphology which could be attributed to different arrangements of TFTPN, ECH, and β-CD during the polymerization.

The polymer appeared as a micron-sized material. The SEM image of β-CD-E-T polymer showed both low and high sphericity angular grain shapes. On the other hand, ZnFe$_2$O$_4$ (Fig. 2b) was observed to form aggregates of particles, giving the appearance of a micron-sized particle. Although the SEM image of ZnFe$_2$O$_4$ revealed that it was agglomerated, it is worth noting that nano-sized particles tend to agglomerate due to surface attractive interactions. The presence of smaller spherical particles within the aggregate indicated that the size of ZnFe$_2$O$_4$ particles was $\sim$30–50 nm. Bright, nano-sized spherical spots were observed on micron-sized granules (Fig. 2c; 200 μm scale), suggesting successful reinforcement of nano-sized ZnFe$_2$O$_4$ in the β-CD-E-T polymer matrix. The enlarged image confirmed the reinforcement of ZnFe$_2$O$_4$ in the polymer matrix.

From BET and Barrett–Joyner–Halenda (BJH) analysis the surface area, pore volume, and pore size of β-CD-E-T/ZnFe$_2$O$_4$ were found to be 6.97 m^2 g^{-1}, 0.0164 cm^3 g^{-1}, and 1.70 nm, respectively.[36] The BJH pore size distribution of β-CD-E-T/ZnFe$_2$O$_4$ is given in Fig. S2.† Depending on pore size, the material can be classified as (i) microporous (pore size < 2 nm), (ii) mesoporous (2 nm < pore size < 50 nm), and (iii) macroporous (pore size > 50 nm).[43] However, from BJH pore size distribution, it was found that both pore size <2 nm and pore size between 2–14 nm were present in the β-CD-E-T/ZnFe$_2$O$_4$

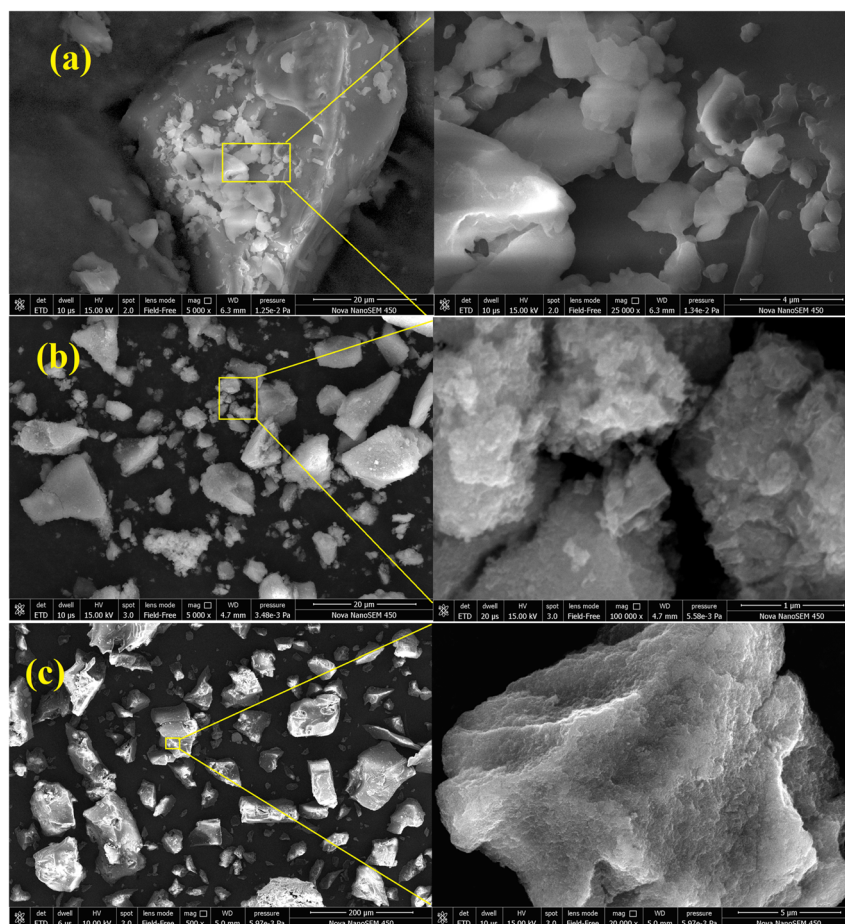**Fig. 2** SEM images of (a) β-CD-E-T, (b) ZnFe$_2$O$_4$, and (c) β-CD-E-T/ZnFe$_2$O$_4$.

nanocomposite. Despite the presence of pores, β-CD-E-T/ZnFe$_2$O$_4$ has a low specific surface area than other porous materials. For example, Li *et al.*,[44] reported that β-CD-Decafluorobiphenyl based polymer show micropores between 1.1–1.7 nm with a high specific surface area of 261.1 m^2 g^{-1}. However, the specific surface area of β-CD-E-T/ZnFe$_2$O$_4$ was higher than that reported for β-CD polymer containing ECH and TFTPN (0.31 m^2 g^{-1}).[26] The wide number of pores and moderate surface area can allow a better interaction between BPA and β-CD-E-T/ZnFe$_2$O$_4$, leading to significant adsorption.

3.2. Thermal studies

The thermal stability of β-CD-E-T and β-CD-E-T/ZnFe$_2$O$_4$ was studied at four heating rates and the corresponding TG-DTG curves are provided in Fig. 3(a–d). Two decomposition steps were observed in the TG curve of β-CD-E-T and β-CD-E-T/ZnFe$_2$O$_4$. The TG curve of both β-CD-E-T (as shown in Fig. 3a) and β-CD-E-T/ZnFe$_2$O$_4$ (as illustrated in Fig. 3c) indicated a substantial mass loss occurring below 230 °C. This mass loss can be attributed to the loss of moisture and volatile content from the surfaces of β-CD-E-T and β-CD-E-T/ZnFe$_2$O$_4$. The first decomposition curve was a common occurrence in the TG curve of β-CD.[45,46] The second step, which exhibited a high mass loss, was identified as the main decomposition step and was attributed to the decomposition of glucopyranose units present in β-

CD. The second decomposition step for both β-CD-E-T and β-CD-E-T/ZnFe$_2$O$_4$ occurred between 200–400 °C, followed by a slow, gradual mass loss up to 600 °C. The first decomposition of β-CD-E-T occurred between 30–220 °C, resulting in a mass loss of 15%. The primary decomposition of β-CD-E-T took place between 221–370 °C, exhibiting a mass loss of 55%. Subsequently, an additional mass loss of 12% was observed up to a temperature of 600 °C. Upon subjecting β-CD-E-T to a higher heating rate, both the TG and DTG curves (as depicted in Fig. 3a and b) shifted towards higher temperatures. The mass loss observed for the first and second decomposition step of β-CD-E-T at a heating rate of 10 °C min^{-1} was 10% and 50%, respectively. At a heating rate of 15 °C min^{-1}, mass losses of 6% and 55% were observed for the first and second decomposition steps, respectively. Similarly, at a heating rate of 20 °C min^{-1}, mass losses of 7% and 55% were observed for the first and second decomposition steps.

The thermal decomposition of pristine β-CD-E-T and β-CD-E-T/ZnFe$_2$O$_4$ was compared, and it was observed that the latter occurred at a slightly lower temperature. As previously discussed, the decomposition pattern of β-CD-E-T/ZnFe$_2$O$_4$ was like that of β-CD-E-T, as ZnFe$_2$O$_4$ is a stable compound and does not undergo additional decomposition. The mass loss in the second decomposition step of β-CD-E-T/ZnFe$_2$O$_4$ was found to be 7–9% less than that of β-CD-E-T polymer at heating rates of
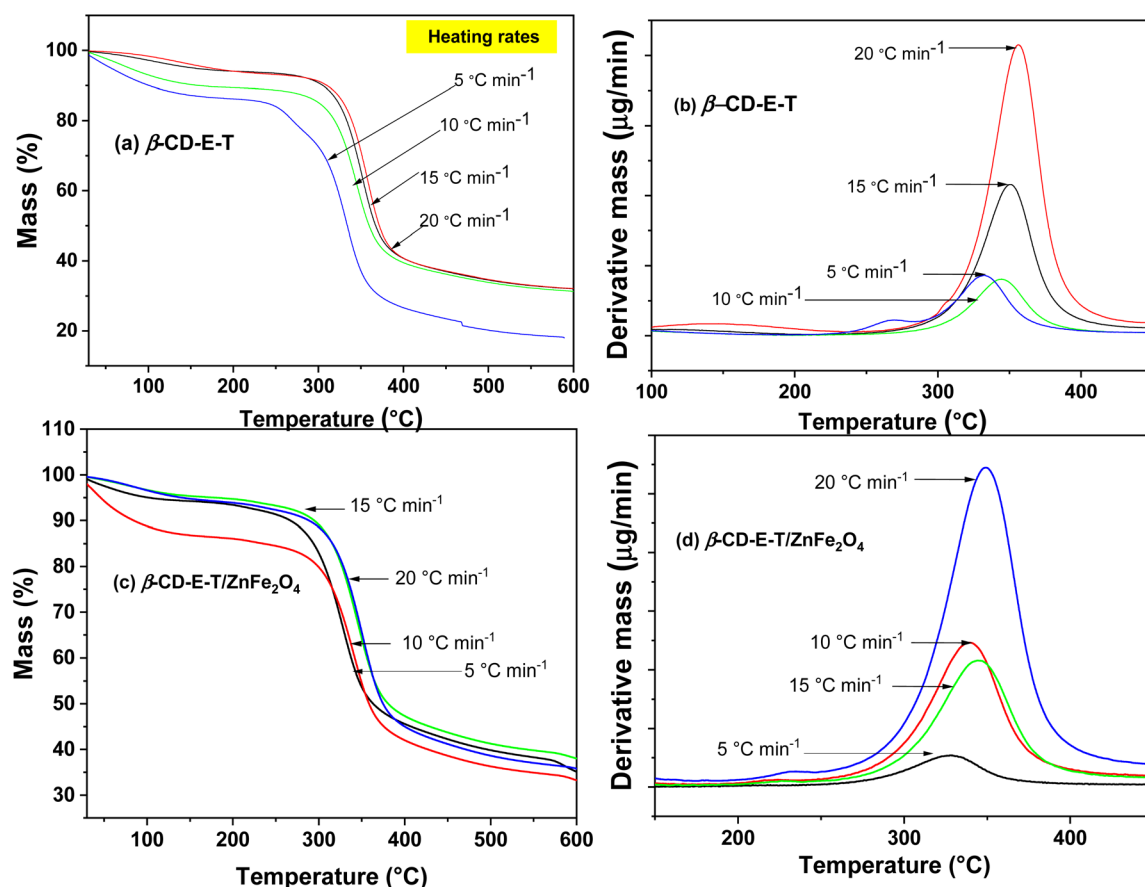

Fig. 3 (a) TG curve of β-CD-E-T, (b) DTG curve of β-CD-E-T, (c) TG curve of β-CD-E-T/ZnFe$_2$O$_4$, and (d) DTG curve of β-CD-E-T/ZnFe$_2$O$_4$.

Table 1 The peak decomposition temperature of β-CD-E-T and β-CD-E-T/ZnFe$_2$O$_4$ at 5, 10, 15, and 20 °C min^{-1} heating rates

Sample	DTG peak decomposition temperature (K) at four heating rates			
	5 K min^{-1}	10 K min^{-1}	15 K min^{-1}	20 K min^{-1}
β-CD-E-T	606	617	623	629
β-CD-E-T/ZnFe$_2$O$_4$	601	612	617	622

10, 15, and 20 °C min^{-1}, which agreed with the ZnFe$_2$O$_4$ reinforcement content. However, a slightly higher mass loss was observed at a heating rate of 5 °C min^{-1}. The peak temperature of the derivative thermogravimetric (DTG) curves of β-CD-E-T/ZnFe$_2$O$_4$ (Fig. 3d) was found to shift to a lower temperature than β-CD-E-T by 5, 5, 6, and 7 K at heating rates of 5, 10, 15, and 20 °C min^{-1}, respectively. This observation indicates that the addition of nano ZnFe$_2$O$_4$ destabilized the β-CD-E-T matrix. Table 1 provides the peak decomposition temperature of the DTG curves of β-CD-E-T and β-CD-E-T/ZnFe$_2$O$_4$ at the four heating rates. It was observed that β-CD-E-T/ZnFe$_2$O$_4$ nanocomposite decomposed at a lower temperature than β-CD-E-T at all heating rates, suggesting that the reinforcement of ZnFe$_2$O$_4$ in β-CD-E-T resulted in matrix destabilization.

However, there are non-isothermal isoconversion methods are available to confirm the thermal degradation of β-CD-E-T and β-CD-E-T/ZnFe$_2$O$_4$ from the activation energy of the decomposition process. To study the thermal degradation, the activation energy of both β-CD-E-T and β-CD-E-T/ZnFe$_2$O$_4$ nanocomposite was calculated using two non-isothermal isoconversion methods namely Flynn–Wall–Ozawa (FWO; eqn (16)) and Kissinger–Akahira–Sunose (KAS; eqn (17)) and two iterative methods (it-FWO; eqn (18) and it-KAS; eqn (19)). The DTG curve of β-CD-E-T at 5 °C min^{-1} heating rate was deconvoluted before the calculations.

$$\ln \beta = \ln \left(\frac{0.0048 A E_\alpha}{g(\alpha) R} \right) - 1.0516 \frac{E_\alpha}{RT} \quad (16)$$

$$\ln \left(\frac{\beta}{T^2} \right) = \ln \left(\frac{AR}{g(\alpha) E_\alpha} \right) - \frac{E_\alpha}{RT} \quad (17)$$

$$\ln \frac{\beta}{H_x} = \ln \left(\frac{0.0048 A E_\alpha}{g(\alpha) R} \right) - 1.0516 \frac{E_\alpha}{RT} \quad (18)$$

$$\ln \left(\frac{\beta}{h_{(x)} T^2} \right) = \ln \left(\frac{AR}{g(\alpha) E_\alpha} \right) - \frac{E_\alpha}{RT} \quad (19)$$

where α, β, A, E_α, and g(α) represent the extent of conversion, heating rate (°C min^{-1}), pre-exponential factor, activation energy at a given extent of conversion (kJ mol^{-1}), and mathematical model, respectively. The value of α, $H_{(x)}$, and $h_{(x)}$ was calculated using eqn (20), (21), and (22), respectively. The extent of conversion at different heating rates is reported in Fig. S3.†

$$\alpha = \frac{m_0 - m_t}{m_0 - m_\infty} = \frac{\Delta m}{\Delta m_{\text{total}}} \quad (20)$$

$$H_{(x)} = \frac{\frac{\exp(-x) h_{(x)}}{x}}{0.0048 \exp(-1.00516 x)} \quad (21)$$

$$h(x) = \frac{x^4 + 18x^3 + 86x^2 + 96x}{x^4 + 20x^3 + 120x^2 + 240x + 120} \quad (22)$$

where, m_0, m_t, and m_∞ represents initial mass, mass at a given time/temperature, and mass at end of the decomposition step, respectively. The value of previously calculated activation energy (using the KAS/FWO method) was used to determine the value of x ($x = E_\alpha/RT$) and iteration was used until the change in the E_α was minimal ($\Delta E_\alpha < 0.001$ kJ mol^{-1}). The value of E_α was calculated from the slope of the plot of ln β, ln β/T^2, ln β/$H_{(x)}$, and ln β/$h_{(x)} T^2$ against 1000/T. All fitted data were calculated with a resolution of α = 0.025 across the range of α = 0.1–0.9. The plots of KAS and FWO for β-CD-E-T polymer and β-CD-E-T/ZnFe$_2$O$_4$ nanocomposite are depicted in Fig. S4.†

The variation in the activation energy of the decomposition of β-CD-E-T and β-CD-E-T/ZnFe$_2$O$_4$ with the extent of conversion along with standard error is given in Fig. 4. Although the thermal decomposition temperature of β-CD-E-T/ZnFe$_2$O$_4$ was lower than that of β-CD-E-T polymer, the activation energy of β-CD-E-T/ZnFe$_2$O$_4$ was found to be higher than that of β-CD-E-T polymer at all extents of conversions between α = 0.1–0.9. Regardless of the isoconversion method used, the change in activation energy was the same, ascending with reaction progress. This suggests that a single mechanism exists for the thermal decomposition of both pristine β-CD-E-T and β-CD-E-T/ZnFe$_2$O$_4$ nanocomposite. The average activation energy of β-CD-E-T and its composite with ZnFe$_2$O$_4$ was calculated using four methods, and the results are presented in Fig. S5.† The average E_α for β-CD-E-T using FWO, KAS, it-FWO, and it-KAS was found to be 180 ± 9, 179 ± 9, 171 ± 9, and 179 ± 9 kJ mol^{-1}, respectively. The incorporation of nanosize ZnFe$_2$O$_4$ into the β-CD-E-T polymer matrix resulted in increased activation energy. The average E_α for β-CD-E-T using FWO, KAS, it-FWO, and it-KAS was found to be 218 ± 14, 219 ± 15, 210 ± 14, and 219 ± 15 kJ mol^{-1}, respectively. The value of E_α suggested that the thermal degradation of β-CD-E-T/ZnFe$_2$O$_4$ nanocomposite was harder compared to β-CD-E-T polymer, as it possessed a higher activation energy barrier than β-CD-E-T polymer. The results of the thermo-kinetic investigations suggest that β-CD-E-T/ZnFe$_2$O$_4$ was less prone to thermal degradation than β-CD-E-T polymer. ZnFe$_2$O$_4$ may have significantly interacted with the functional groups of β-CD-E-T polymer, leading to the formation of a new β-CD-E-T/ZnFe$_2$O$_4$ phase with delayed thermal degradation. ZnFe$_2$O$_4$ may have decreased the mobility of the β-CD-E-T polymer chains, physically interacted with the surface of
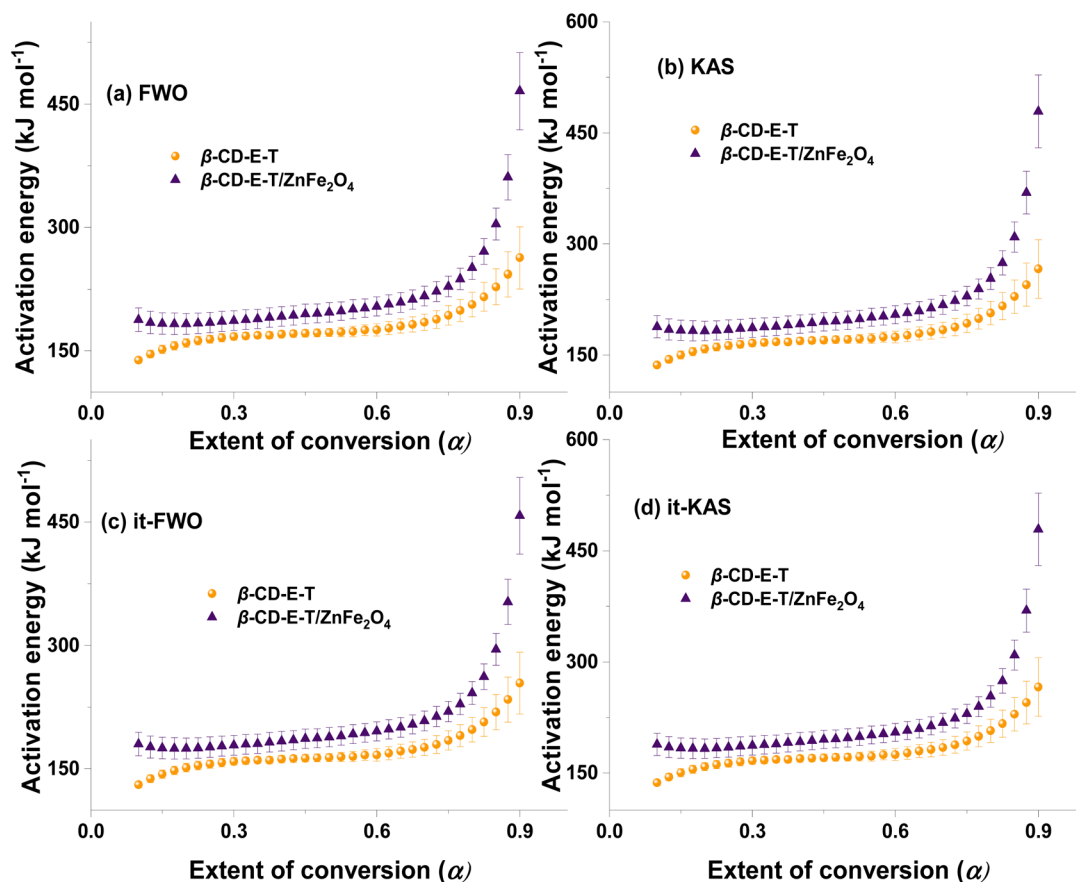
Fig. 4 Variation in the activation energy of the thermal decomposition of β-CD-E-T and β-CD-E-T/ZnFe$_2$O$_4$ calculated using (a) FWO, (b) KAS, (c) it-FWO, and (d) it-KAS with the extent of conversion.

β-CD-E-T, and generated a highly stable zone that aided in decreasing the activation energy of thermal decomposition.[47]

3.3. Effect of different parameters

The pH level plays a crucial role in determining the adsorption of contaminants onto the adsorbent surface. Variations in pH have a direct impact on the surface charge of the adsorbent, which in turn influences the ionic attraction and repulsion forces between the adsorbent and adsorbate, thereby significantly contributing to the adsorption process. To investigate the impact of pH on the adsorption process, several parameters including adsorbent dosage, contact time, the volume of BPA, temperature, and concentration were kept constant, while only the pH levels were varied (pH values of 3, 4, 6, 8, and 10 were used).

The investigation of various pH levels (as shown in Fig. 5a) revealed that the β-CD-E-T/ZnFe$_2$O$_4$ nanocomposite displayed a negative surface charge across all conditions (pH > 2.44; negative charge).[36] It is worth noting that the pK_a range of BPA was estimated to be between 9.6 and 10.2.[48,49] When the pH value exceeded the pK_a of BPA, the hydroxyl groups of BPA underwent deprotonation, resulting in a predominantly negative charge. Conversely, at pH levels below the pK_a of BPA, the compound did not exhibit any charge, either positive or

negative, and remained neutral. Effect of pH (BPA solution volume = 20 mL; T = 28 °C; β-CD-E-T/ZnFe$_2$O$_4$ dose = 10 mg; BPA solution concentration = 32 mg L^{-1}; t = 30 min) on the removal of BPA from the aqueous solution is depicted in Fig. 5a. Initially, there were no significant changes in the adsorption behavior of BPA onto the β-CD-E-T/ZnFe$_2$O$_4$ nanocomposite observed up to a pH of 8, except for a 7% drop in removal percentage observed at pH 4. The adsorption of BPA at pH values of 3, 6, and 8 was approximately 87%, corresponding to a q_e value of around 56 mg g^{-1}. However, a substantial decrease in BPA adsorption was observed at pH 10 compared to pH values between 3 and 8. Specifically, the β-CD-E-T/ZnFe$_2$O$_4$ nanocomposite exhibited only ~55% BPA adsorption (q_e of ~35 mg g^{-1}) at pH 10. The observed decrease in the removal percentage of BPA at pH 10 can be plausibly explained by the negatively charged deprotonated BPA species. Due to the repulsive forces between the negative surface of β-CD-E-T/ZnFe$_2$O$_4$ and the negative charge of BPA, it becomes more difficult for the deprotonated BPA molecules to approach and interact with the adsorbent, leading to a reduced removal efficiency.[26,39,40,50,51] This repulsive force is absent between the neutral BPA molecules and β-CD-E-T/ZnFe$_2$O$_4$ adsorbent at pH levels below 10. Since the maximum adsorption of BPA occurred when it was not charged, it is reasonable to infer that the
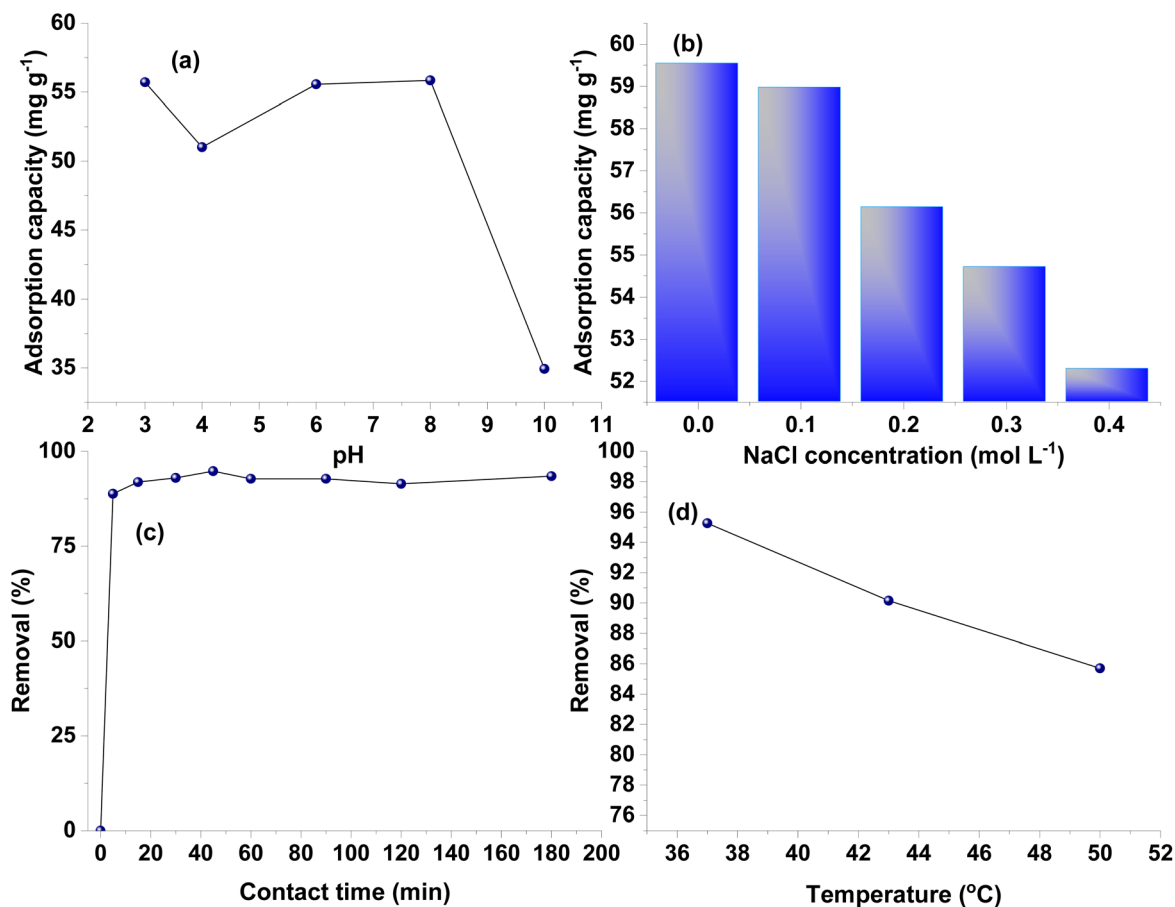
Fig. 5 Effect of (a) pH, (b) ionic salt concentration, (c) contact time, and (d) temperature on the adsorption of BPA by β-CD-E-T/ZnFe$_2$O$_4$ from aqueous solution.

interaction between BPA and β-CD-E-T/ZnFe$_2$O$_4$ was not primarily driven by ionic attraction.[52]

Moreover, the effect of ionic salt on the removal of BPA was tested (Fig. 5b). The removal percentage of BPA was studied in the presence of 0.1, 0.2, 0.3, and 0.4 mol L^{-1} sodium chloride (NaCl) solution and the rest of the parameters were unchanged during the measurement (BPA solution volume = 10 mL; T = 28 °C; β-CD-E-T/ZnFe$_2$O$_4$ dose = 5 mg; BPA solution concentration = 32 mg L^{-1}; t = 30 min). The adsorption of BPA onto β-CD-E-T/ZnFe$_2$O$_4$ was found to be higher in the absence of any ionic salt *i.e.*, NaCl, which was attributed to the strong interaction between the β-CD-E-T/ZnFe$_2$O$_4$ surface and BPA due to availability of more adsorption sites. However, as the ionic concentration of NaCl was increased, the adsorption of BPA decreased. This can be plausibly explained by the fact that as the concentration of ionic salt increases, Na^{1+}, and Cl^{1-} ions can occupy the active adsorption sites and pores on β-CD-E-T/ZnFe$_2$O$_4$ nanocomposite, resulting in fewer active sites available for the adsorption of BPA, and hence, a decreased adsorption percentage of BPA was observed. Nevertheless, it is noteworthy that the decrease in BPA removal was relatively minor, with the removal percentage dropping from 93% (59.6 mg g^{-1}) in the absence of NaCl to approximately 82% (52.2 mg g^{-1}) in the presence of 0.4 mol L^{-1} NaCl. These results indicate that BPA can still be effectively removed even in the presence of Na^{1+} and Cl^{1-} ions, which are often present in wastewater. Furthermore, the outcomes of the ionic salt effect experiments suggest that the absorption of BPA by β-CD-E-T/ZnFe$_2$O$_4$ was not driven by electrostatic attraction, which is consistent with the findings obtained from the pH experiments. Had the electrostatic interaction between β-CD-E-T/ZnFe$_2$O$_4$ and BPA been substantial, a marked reduction in the adsorption capacity would have been observed. For example, in our prior research,[36] we observed a substantial decline in the removal of malachite green dye as the sodium chloride concentration increased, which was attributed to the electrostatic interaction between the adsorbent and malachite green. No such decline was observed in the case of BPA adsorption onto β-CD-E-T/ZnFe$_2$O$_4$. Hence, electrostatic interaction between BPA and β-CD-E-T/ZnFe$_2$O$_4$ nanocomposite was insignificant.

The effect of β-CD-E-T/ZnFe$_2$O$_4$ dose and BPA dose was investigated, and the results are shown in Fig. S6 (ESI File).† The β-CD-E-T/ZnFe$_2$O$_4$ dose was varied between 5 and 100 mg while keeping other parameters constant (BPA solution volume = 20 mL; T = 28 °C; BPA solution concentration = 32 mg L^{-1}; t = 30 min; pH = 6; β-CD-E-T/ZnFe$_2$O$_4$ dose = varied). Similarly, to study the effect of BPA dose on the adsorption of BPA on β-CD-E-T/ZnFe$_2$O$_4$, the BPA dose was varied between 0.2 and 1.6 mg

while keeping other parameters constant ($T = 28$ °C; $t = 30$ min; pH = 6; β-CD-E-T/ZnFe$_2$O$_4$ dose = 5 mg; BPA dose = varied). At low β-CD-E-T/ZnFe$_2$O$_4$ doses (*i.e.*, 5 mg and 10 mg), nano-composite exhibited significant adsorption for BPA (>85%). However, thereafter, the removal % of BPA drops significantly with increasing β-CD-E-T/ZnFe$_2$O$_4$ dose. This could be attributed to the fact that at low β-CD-E-T/ZnFe$_2$O$_4$ doses, the adsorbent particles are not agglomerated, resulting in more interaction between the active surface of β-CD-E-T/ZnFe$_2$O$_4$ and a larger number of pores being available for adsorption of BPA. However, at higher β-CD-E-T/ZnFe$_2$O$_4$ doses, a greater number of moles of β-CD-E-T/ZnFe$_2$O$_4$ are present in the same volume of BPA solution, which can lead to increased collision/interaction between β-CD-E-T/ZnFe$_2$O$_4$ adsorbent–adsorbent molecules. This may result in the formation of agglomerates of β-CD-E-T/ZnFe$_2$O$_4$, leading to a decrease in available surface area and pores for BPA-β-CD-E-T/ZnFe$_2$O$_4$ interaction in the solution, thereby decreasing the overall BPA removal percentage at higher β-CD-E-T/ZnFe$_2$O$_4$ loadings. Therefore, since the BPA removal efficiency was almost the same for both 5 mg and 10 mg β-CD-E-T/ZnFe$_2$O$_4$ loading, the lower loading of 5 mg β-CD-E-T/ZnFe$_2$O$_4$ was found to be the most appropriate dose for β-CD-E-T/ZnFe$_2$O$_4$.

The R% of BPA was decreased by increasing the BPA dose in the solution from 0.2 to 1.2 mg (Fig. S6†). However, the adsorption capacity of β-CD-E-T/ZnFe$_2$O$_4$ was continuously increased between 0.2 and 1.2 mg BPA dose. The adsorption capacity of β-CD-E-T/ZnFe$_2$O$_4$ for BPA varied from 27.8 mg g^{-1} at 0.2 mg BPA dose to 204.6 mg g^{-1} at 1.2 BPA dose. After 1.2 mg BPA content, a decline in the adsorption capacity was observed. The removal % of BPA remained >85% up to 0.64 mg BPA dose. The decrease in the adsorption capacity observed at high BPA concentrations was attributed to the saturation of active adsorption sites available on β-CD-E-T/ZnFe$_2$O$_4$ for BPA adsorption.

The effect of contact time on the R% of BPA is depicted in Fig. 5c. The effect of contact time was investigated under defined parameters (BPA solution volume = 20 mL; $T = 28$ °C; BPA solution concentration = 32 mg L^{-1}; β-CD-E-T/ZnFe$_2$O$_4$ dose = 5 mg; $t = 0$–180 minutes; pH = 6). Very rapid adsorption of BPA onto the β-CD-E-T/ZnFe$_2$O$_4$ nanocomposite surface was observed, with over 85% BPA adsorbed within 5 minutes. This can be attributed to the higher availability of BPA molecules, resulting in more collisions between the adsorbent–adsorbate and adsorbate–adsorbate molecules. At pH = 6, the BPA molecules could easily approach the surface of the β-CD-E-T/ZnFe$_2$O$_4$ nanocomposite because of their neutral charge and get adsorbed, leading to an increase in BPA concentration on the nanocomposite's surface and a decrease in freely movable BPA molecules in the aqueous solution. The adsorbed BPA molecules occupy active sites on the β-CD-E-T/ZnFe$_2$O$_4$'s surface, reducing the availability of active sites for approaching BPA molecules in the solution. As a result, BPA adsorption on β-CD-E-T/ZnFe$_2$O$_4$ slowed down significantly after 5 minutes, with only a 4% increase in removal observed between 5 and 30 minutes. Equilibrium was established thereafter, and no significant variation in BPA removal percentage was observed

up to 180 minutes. Consequently, a contact time of 30 minutes was selected for the subsequent experimental measurements. The contact time data was then fitted using four kinetic models to obtain a more comprehensive understanding of the adsorption kinetics of BPA onto the β-CD-E-T/ZnFe$_2$O$_4$ nanocomposite.

To calculate the thermodynamic parameters concerning the adsorption process, the effect of temperature on the adsorption of BPA on β-CD-E-T/ZnFe$_2$O$_4$ adsorbent was investigated under standard conditions (BPA solution volume = 20 mL; T = varied; BPA solution concentration = 32 mg L^{-1}; β-CD-E-T/ZnFe$_2$O$_4$ dose = 5 mg; time = 30 minutes; pH = 6). Fig. 5d illustrates the changes in the BPA R% at three different temperatures. It was observed that the BPA R% decreased with an increase in temperature, indicating an exothermic nature of the adsorption process. The decline in the BPA removal percentage with increasing temperature was attributed to a greater number of BPA molecules being desorbed from the β-CD-E-T/ZnFe$_2$O$_4$'s surface than those being adsorbed onto it.[53] A decrease in BPA removal efficiency with rising temperatures was noted in prior investigations examining the efficacy of covalent organic frameworks and mesoporous-activated carbon for BPA removal.[19,53] This behavior is typically observed in physical adsorption processes, where the desorption rate increases with temperature. It can be inferred that the adsorption of BPA onto β-CD-E-T/ZnFe$_2$O$_4$ nanocomposite was primarily governed by physical interactions. The thermodynamic parameters like $\Delta S°$, $\Delta H°$, and $\Delta G°$ were calculated by fitting experimental data to get more insight into the adsorption nature.

3.4. Kinetics, isotherm, and thermodynamic studies

The kinetics of the adsorption process was used to define the rate of BPA adsorption by β-CD-E-T/ZnFe$_2$O$_4$ adsorbent, and various kinetic models were employed to analyze experimental data to explain the adsorption process. A total of four kinetic models were used to get insight into the kinetic process of adsorption. The kinetic plots are given in Fig. 6(a–d) and the corresponding results are reported in Table 2. Among the four kinetic models, the pseudo-second-order kinetic model was the best-suited (correlation coefficient $R^2 = 0.999$) model to describe the kinetics of the uptake of BPA by β-CD-E-T/ZnFe$_2$O$_4$. A very good equilibrium adsorption capacity of 121 ± 1 mg g^{-1} was obtained using a pseudo-second-order fit, which was closer to the experimental value (122 ± 1 mg g^{-1}). The correlation coefficient for BPA adsorption by β-CD-E-T/ZnFe$_2$O$_4$ was poor for the intraparticle diffusion model and Elovich model suggesting that the intraparticle diffusion was not rate-determining the adsorption process. The high value of k_2 suggested a very fast adsorption of BPA onto β-CD-E-T/ZnFe$_2$O$_4$.

The knowledge of adsorption isotherm is critical for planning and optimizing BPA adsorption on β-CD-E-T/ZnFe$_2$O$_4$ nanocomposite, as well as understanding the underlying adsorption mechanism (*i.e.*, multilayer, monolayer, chemosorption, physisorption, favourability of the BPA adsorption).[54] Adsorption isotherm models were used among the four isotherm models, all models were showing good linear fit (Fig. 7a–d; $R^2 = 0.967$–0.994). Hence, the adsorption of BPA
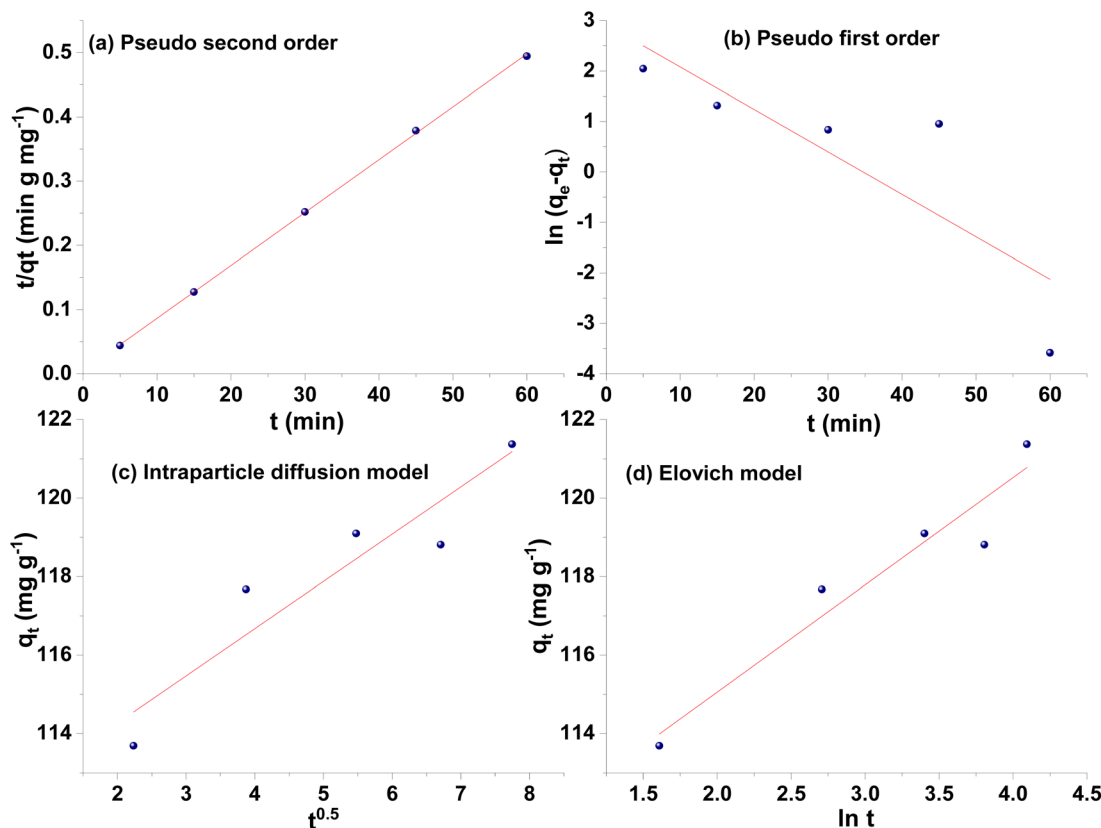
Fig. 6 Adsorption kinetics plots of BPA adsorption onto β-CD-E-T/ZnFe$_2$O$_4$: (a) pseudo-second-order, (b) pseudo-first-order, (c) intraparticle diffusion, and (d) Elovich plot.

Table 2 Kinetics parameters of adsorption of BPA onto β-CD-E-T/ZnFe$_2$O$_4$ nanocomposite

Kinetic model	Parameter	BPA
Pseudo-first order	k_1 (min^{-1})	0.194 ± 0.073
	$q_{e,cal}$ (mg g^{-1})	18.5 ± 12.8
	R^2	0.701
Pseudo-second order	$q_{e,exp}$	122 ± 1
	k_2 (g mg^{-1} min^{-1})	0.0157 ± 0.0062
	$q_{e,cal}$ (mg g^{-1})	121 ± 1
	R^2	0.999
Intraparticle diffusion	k_p (mg g^{-1} min$^{-0.5}$)	1.20 ± 0.26
	C (mg g^{-1})	112 ± 1
	R^2	0.881
Elovich	a (mg g^{-1} min^{-1})	24.7 ± 4.3
	b (g mg^{-1})	$(7.07 \pm 2.9) \times 10^{17}$
	R^2	0.926

could have been due to many possible mechanisms. A high Langmuir maximum adsorption capacity of 270 ± 36 mg g^{-1} (Table 3) was obtained for the removal of BPA using β-CD-E-T/ZnFe$_2$O$_4$ nanocomposite. The Freundlich isotherm proved to be the most suitable model ($R^2 = 0.994$) for describing the adsorption process, indicating that the adsorption of BPA onto the heterogeneous β-CD-E-T/ZnFe$_2$O$_4$ surface occurred *via* multilayer adsorption. The high value of Freundlich constant n (1.63 ± 0.07) suggested the adsorption process was highly

favorable ($n > 1$).[29] The obtained factor n value provided further support for the high Langmuir adsorption capacity observed. Additionally, the calculated R_L value of 0.155 ($0 < R_L < 1$), indicated favorable adsorption of BPA onto the β-CD-E-T/ZnFe$_2$O$_4$ surface. Based on the results obtained from the Dubinin–Radushkevich model, the calculated adsorption energy value of 5.87 ± 0.19 kJ mol^{-1} was found to be lower than the threshold of 8 kJ mol^{-1}, suggesting that the adsorption of BPA onto the β-CD-E-T/ZnFe$_2$O$_4$ nanocomposite was primarily a physical process.[54]

The analysis of the temperature effects revealed that the adsorption of BPA onto the β-CD-E-T/ZnFe$_2$O$_4$ adsorbent was characterized by an exothermic nature. To confirm this ΔS° and ΔH° were calculated from the interception and slope of the plot given in Fig. S7† (eqn (12)), respectively. From the calculation of the thermodynamic parameters, it was found that the value of ΔH° and ΔS° for the adsorption of BPA onto the β-CD-E-T/ZnFe$_2$O$_4$ was -77.1 ± 16.0 kJ mol^{-1} and -0.213 ± 0.051 kJ mol^{-1} K^{-1}, respectively. $0 > \Delta H^\circ$ (negative) confirms the exothermic nature of the adsorption process. The negative value of ΔS° ($0 > \Delta S^\circ$) indicated a reduction in randomness or an increase in the orderliness of the system after BPA adsorption onto the β-CD-E-T/ZnFe$_2$O$_4$ adsorbent. The calculated values of ΔG°, ranging from -11.1 to -8.36 kJ mol^{-1} with an average of -9.78 kJ mol^{-1}, were also found to be negative, indicating that the adsorption of BPA onto the β-CD-E-T/ZnFe$_2$O$_4$ surface
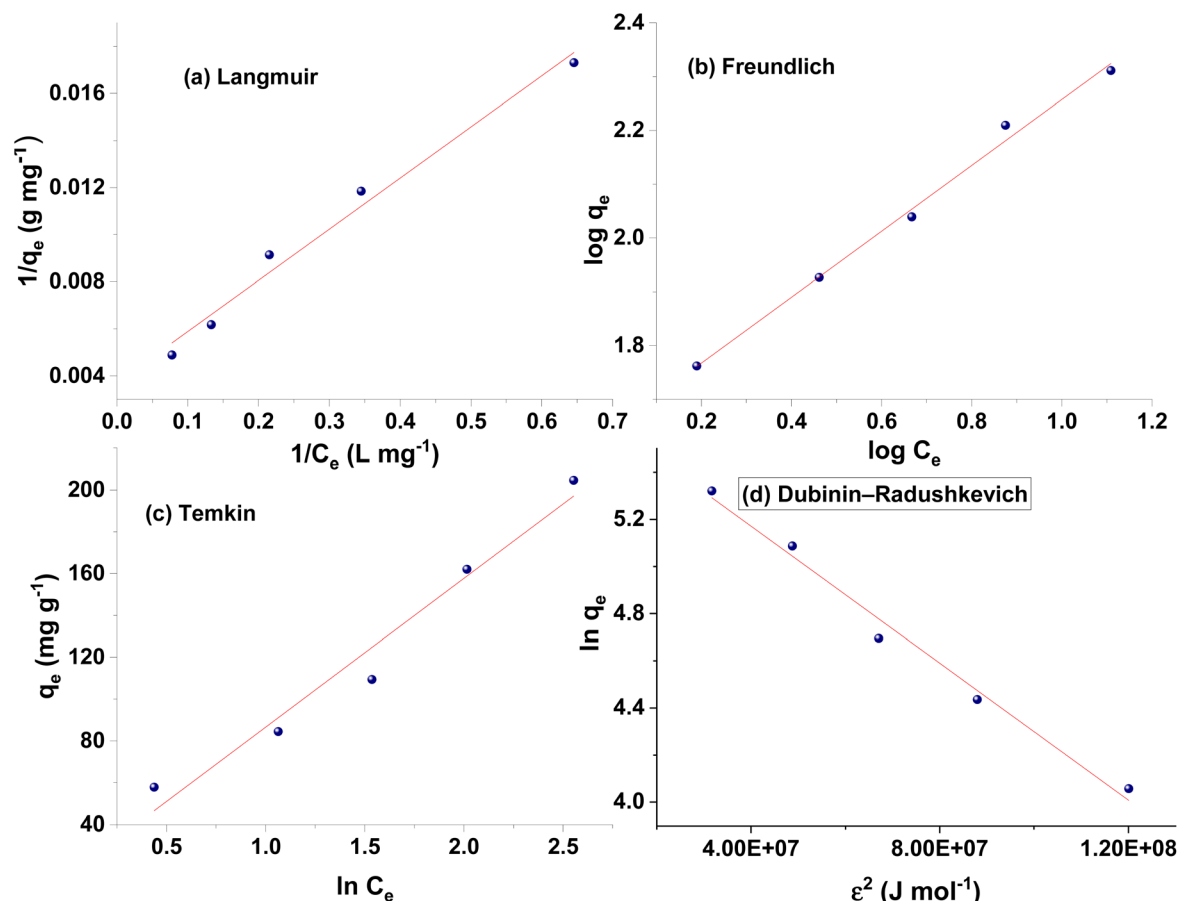
Fig. 7 Adsorption isotherms plots of BPA adsorption onto β-CD-E-T/ZnFe$_2$O$_4$: (a) Langmuir, (b) Freundlich, (c) Temkin, and (d) Dubinin–Radushkevich plot.

Table 3 Isotherms parameters of the adsorption of BPA onto β-CD-E-T/ZnFe$_2$O$_4$ nanocomposite

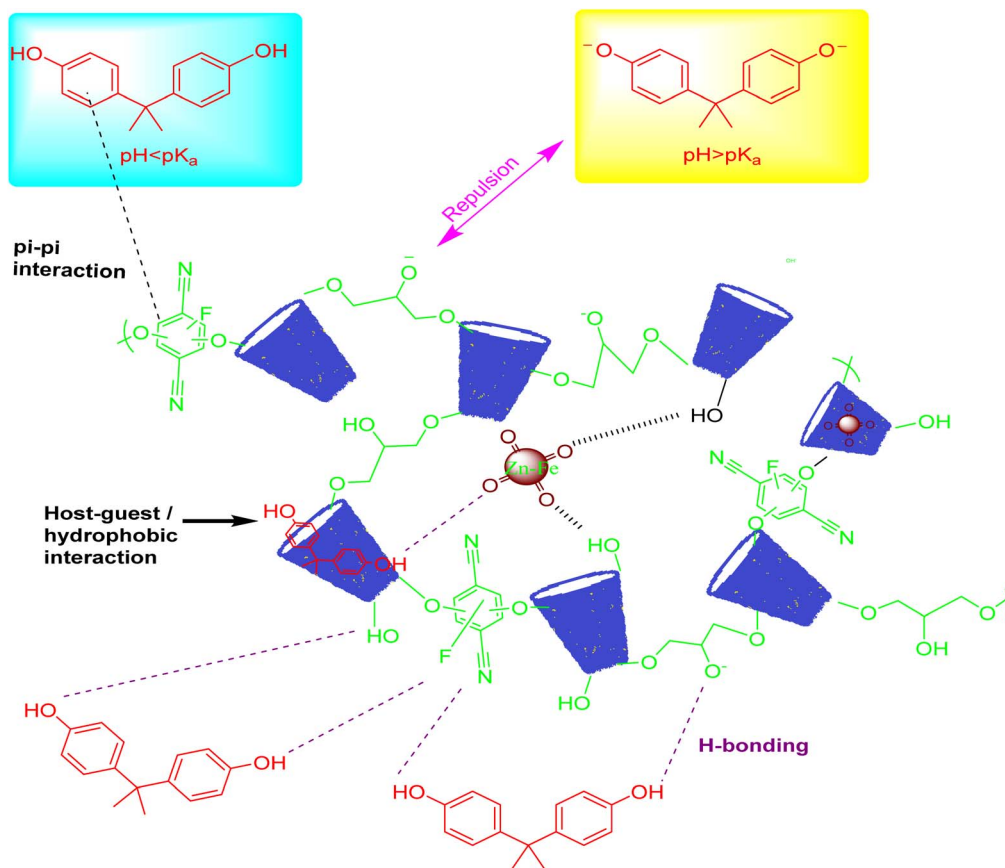| Model	Parameter	BPA
Langmuir	$q_{m,exp}$ (mg g^{-1})	205 ± 2
	q_m (mg g^{-1})	270 ± 36
	K_L (L mg^{-1})	0.171 ± 0.012
	R^2	0.984
Freundlich	K_F (mg g^{-1} (L mg^{-1})$^{1/n}$)	44.1 ± 2.0
	$1/n$	0.613 ± 0.028
	R^2	0.994
Temkin	A_T (L g^{-1})	1.24 ± 0.20
	b_T (kJ mol^{-1})	35.4 ± 3.4
	R^2	0.967
Dubinin–Radushkevich	q_m (mol g^{-1})	315 ± 23
	δ (mol^2 J^2)	(1.45 ± 0.10) × 10^{-8}
	E (kJ mol^{-1})	5.87 ± 0.19
	R^2	0.987

occurred spontaneously without the requirement of additional energy. The high negative value ΔG° at the low temperature suggested that the adsorption of BPA was more spontaneous at low temperatures.[29] Fu *et al.* has reported that adsorption of BPA on imine-based covalent organic frameworks was an exothermic process with $\Delta H^{\circ} = -37.1$ kJ mol^{-1}, $\Delta S^{\circ} = -0.109$ kJ mol^{-1} K^{-1}, and $\Delta G^{\circ} = -4.24$ to -1.95 kJ mol^{-1}.[19] The more negative value of ΔG° implied more favorable adsorption of BPA onto β-CD-E-T/ZnFe$_2$O$_4$ than imine based covalent organic frameworks, which was confirmed by the higher adsorption of BPA onto β-CD-E-T/ZnFe$_2$O$_4$.

3.5. Plausible adsorption mechanism

Based on the results obtained from FTIR, isotherm, kinetics, and thermodynamics analyses, it was evident that the high adsorption capacity of β-CD-E-T/ZnFe$_2$O$_4$ for BPA was primarily attributed to physical adsorption. Moreover, the adsorption of BPA by β-CD-E-T/ZnFe$_2$O$_4$ was found to be unaffected by pH levels ranging from 3–8 and the presence of ionic salts, indicating that ionic interactions between the β-CD-E-T/ZnFe$_2$O$_4$ adsorbent and BPA adsorbate were not the main driving force responsible for the adsorption. Instead, the adsorption of BPA onto β-CD-E-T/ZnFe$_2$O$_4$ was primarily driven by hydrogen bonding, π–π interaction, and host–guest/hydrophobic interactions, as suggested by the FTIR studies (Scheme 1).[19,27,29] Furthermore, it is possible that the cross-linking material caused the formation of secondary cavities within the polymer network, which facilitated the sequestration of BPA molecules within these cavities. In addition, the moderate specific surface area of β-CD-E-T/ZnFe$_2$O$_4$ provided a greater number of available adsorption sites for the binding of BPA.[27]

Scheme 1 Proposed interactions responsible for the adsorption of BPA onto β-CD-E-T/ZnFe₂O₄.

3.6. Regeneration performance of β-CD-E-T/ZnFe₂O₄ nanocomposite

The β-CD-E-T/ZnFe₂O₄ nanocomposite was subjected to five regeneration–reuse cycles to evaluate its stability and reusability. As shown in Fig. 8, a significant decrease in the adsorption capacity of β-CD-E-T/ZnFe₂O₄ for BPA was observed after each regeneration–reuse cycle. The adsorption capacity decreased by 25.6%, 49.1%, and 57.0% after the first, third, and fifth cycles, respectively, with a final adsorption capacity of only 85.6 ± 3.3 mg g^{-1}. This reduction in adsorption capacity may be attributed to the stronger binding between BPA and β-CD-E-T/ZnFe₂O₄ adsorbent. The strong interaction between the adsorbent and adsorbate resulted in reduced desorption of BPA molecules, leading to a high decrement in adsorption capacity with subsequent regeneration/reuse cycles. Despite this decrease, the adsorption capacity of β-CD-E-T/ZnFe₂O₄ after the fifth cycle ($q_e > 85$ mg g^{-1}) was still higher than that reported for other β-CD-containing adsorbents, such as carboxymethyl-β-CD/Fe₃O₄ composite, β-CD capped graphene-magnetite nanocomposite, and polyethylenimine–polyethylene glycol-β-CD polymer.[27,29,30] These findings indicate that the β-CD-E-T/ZnFe₂O₄ nanocomposite could be reused to a certain extent.

3.7. Comparative adsorption performance

The adsorption performance of β-CD-E-T/ZnFe₂O₄ nanocomposite was compared with previously reported adsorbents for the removal of BPA (Table 4).[13,19,26–30,39,40,50–53,55–58] As reported in Table 4, β-CD based adsorbents like carboxymethyl-β-CD polymer/Fe₃O₄ composite, β-CD/graphene-magnetite nanocomposite, and polyethylenimine-polyethylene glycol-β-CD polymer were not very effective for the BPA elimination from the aqueous solution.[27,29,30] The β-CD based polymer and
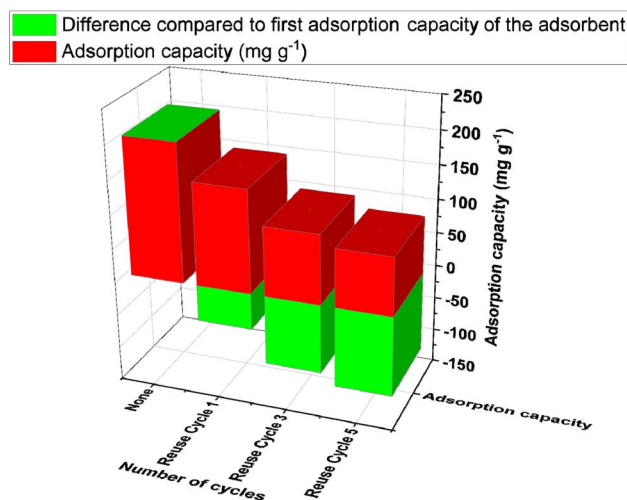

Fig. 8 Adsorption capacity of β-CD-E-T/ZnFe₂O₄ nanocomposite adsorbent for BPA after number of regeneration reuse cycles.

Table 4 Comparison of adsorption performance of various adsorbents towards BPA removal

Adsorbent	q_m (mg g^{-1})	q_e (mg g^{-1})	Equilibrium time (min)	Ref.
β-CD-E-T/ZnFe$_2$O$_4$ nanocomposite	270 ± 36	122 ± 1	30	Present work
Zeolite-imidazolate-framework-8@mesoporous silica (SBA-15)	135	123	2	52
Activated carbon from hydro-char	21.3	14.2	240	50
Partially reduced GO	346	[a]NA	1080	55
Mesoporous silica nanoparticles functionalized with hexadecyltrimethylammonium	128	80.5 ± 3.7	60	51
Imine-based covalent organic framework (COF-2)	149	116	60	19
PAF-82	689	[a]NA	15	56
Polyethylenimine-polyethylene glycol-β-CD polymer	65.3	60.1	1140	30
Sludge-based mesoporous activated carbon (SS-HP)	153	88.8	60	53
Carboxymethyl-β-CD polymer/Fe$_3$O$_4$	74.6	60.8	250	27
L-Glutamic acid modified GO (GO-Glu)	237 ± 40	[a]NA	<60	57
GO/cross-linked chitosan/magnetite (GO–CSm)	86.2	81.3	60	39
N/S doped magnetic carbon aerogel	200	197	120	58
β-CD capped graphene-magnetite nanocomposite	66.0	NA	240	29
Iron oxide/graphene aerogel	254	216	480	40
β-CD-4,4′-bis(chloromethyl) biphenyl polymer	139	38.0	10	28
TFTPN-ECH-β-CD polymer	118	21.9	10	26
Activated carbon	91.9	43.1	2880	13
Magnetic reduced GO (MRGO-1)	93.0	60.9	240	60

[a] NA = not available.

composites were having a maximum uptake of 65–139 mg BPA per 'g' of adsorbent used. Compared to that the β-CD-E-T/ZnFe$_2$O$_4$ nanocomposite synthesized in the present work exhibited a very good BPA adsorption (195–205 mg g^{-1} more adsorption than reported β-CD based adsorbents in Table 4).[27,29,30] The reported β-CD based adsorbents exhibited very slow adsorption compared to β-CD-E-T/ZnFe$_2$O$_4$ nanocomposite, except β-CD-4,4′-bis(chloromethyl) biphenyl and TFTPN-ECH-β-CD polymer.[28] N/S doped magnetic carbon aerogel, iron oxide/graphene aerogel, partially reduced GO, L-glutamic acid modified GO and porous aromatic framework (PAF) were reported to show a very good adsorption efficiency for BPA.[40,55–58] However, very slow adsorption was observed for partially reduced GO, iron oxide/graphene aerogel and N/S doped magnetic carbon aerogel. PAF-82 exhibited a faster and high good adsorption capacity for BPA removal. PAF-82 reported by Mo et al.[56] exhibited a very high adsorption performance due to its high specific surface area (1073 mg g^{-1}) and higher porous structure than β-CD-E-T/ZnFe$_2$O$_4$ nanocomposite. It is important to emphasize that a high specific surface area alone does not necessarily translate into greater adsorption efficiency. Effective adsorption relies on the presence of proper interactions between the adsorbate (BPA) and the adsorbent. For instance, despite having a significantly higher specific surface area (1200 m^2 g^{-1}; ~172 times), the activated carbon reported by Martín-Lara et al.[13] exhibited lower BPA adsorption compared to the β-CD-E-T/ZnFe$_2$O$_4$ nanocomposite described in this study. Furthermore, Supong et al.[59] also reported low adsorption capacity (q_m = 15.7 mg g^{-1}) for the activated carbon, despite its surface area being about ~123 times greater than that of the β-CD-E-T/ZnFe$_2$O$_4$ adsorbent. This discrepancy suggests that specific interactions between BPA and activated carbon may be lacking, unlike those observed between BPA and the β-CD-E-T/ZnFe$_2$O$_4$ nanocomposite. However, it is worth noting that within adsorbent materials possessing a similar composition, a high specific surface area can indeed contribute to enhanced BPA adsorption.[56,60]

In conclusion, despite the moderate surface area and decrease in adsorption performance observed after the fifth cycle, the β-CD-E-T/ZnFe$_2$O$_4$ nanocomposite demonstrated a higher maximum adsorption capacity than many pristine materials reported in Table 4. This makes β-CD-E-T/ZnFe$_2$O$_4$ nanocomposite a better adsorbent for the faster removal of BPA from an aqueous solution.

4. Conclusions

The thermo-kinetic investigations suggested that the β-CD-E-T/ZnFe$_2$O$_4$ nanocomposite was less prone to thermal degradation than the β-CD-E-T polymeric matrix due to the high activation energy barrier required for its thermal degradation. The adsorption studies confirmed that β-CD-E-T/ZnFe$_2$O$_4$ exhibited a high affinity towards BPA (q_m = 270 ± 36 mg g^{-1}) and achieved a high equilibrium adsorption capacity within a short time of 30 minutes. However, the removal of BPA decreased under highly alkaline conditions and at higher temperatures. The thermodynamic and isotherm investigations suggested that BPA adsorption onto the heterogeneous β-CD-E-T/ZnFe$_2$O$_4$ surface was a spontaneous, exothermic, multilayer physical adsorption process. Furthermore, β-CD-E-T/ZnFe$_2$O$_4$ was effective in removing BPA from aqueous solutions, even in the presence of ionic salt like sodium chloride. The ionic effect and pH studies indicated that ionic interaction was not the main interaction between β-CD-E-T/ZnFe$_2$O$_4$ and BPA responsible for

the adsorption. The FTIR studies suggested that the adsorption of BPA onto β-CD-E-T/ZnFe$_2$O$_4$ was accompanied by strong hydrogen bonding, π–π interaction, and hydrophobic/host–guest interaction. One disadvantage of using the β-CD-E-T/ZnFe$_2$O$_4$ adsorbent for BPA removal was a drastic decrease in the adsorption efficiency of recycled β-CD-E-T/ZnFe$_2$O$_4$. However, despite this decrease, β-CD-E-T/ZnFe$_2$O$_4$ still exhibited a higher adsorption capacity than some of the as-synthesized adsorbent materials, making it a cost-effective adsorbent material.

Data availability

The data supporting the study's conclusions are included in the publication and its ESI.†

Author contributions

RS contributed to the conceptualization, methodology, data collection, data curation, and writing the original draft. PND supervised the research, edited and reviewed the original draft, and finalized the manuscript.

Conflicts of interest

The authors declare no known conflict of interest.

Acknowledgements

References

1 A. Shafei, M. Matbouly, E. Mostafa, S. Al Sannat, M. Abdelrahman, B. Lewis, B. Muhammad, S. Mohamed and R. M. Mostafa, *Environ. Sci. Pollut. Res.*, 2018, **25**, 23624–23630.

2 J. Moreman, O. Lee, M. Trznadel, A. David, T. Kudoh and C. R. Tyler, *Environ. Sci. Technol.*, 2017, **51**, 12796–12805.

3 S. A. Krieg, L. K. Shahine and R. B. Lathi, *Fertil. Steril.*, 2016, **106**, 941–947.

4 H.-J. Lehmler, B. Liu, M. Gadogbe and W. Bao, *ACS Omega*, 2018, **3**, 6523–6532.

5 M. Fürhacker, S. Scharf and H. Weber, *Chemosphere*, 2000, **41**, 751–756.

6 Y. Xu, Y. Wu, S. Hyun Hur, S. Ho Hong, W.-S. Choe and I.-K. Yoo, *ChemistrySelect*, 2022, **7**, e202204102.

7 C. Brahmi, M. Benltifa, M. Ghali, F. Dumur, C. Simonnet-Jégat, V. Monnier, F. Morlet-Savary, L. Bousselmi and J. Lalevée, *J. Appl. Polym. Sci.*, 2021, **138**, 50864.

8 Z. Pan, F. Yu, L. Li, C. Song, J. Yang, C. Wang, Y. Pan and T. Wang, *Sep. Purif. Technol.*, 2019, **227**, 115695.

9 Y. Jia, A. Eltoukhy, J. Wang, X. Li, T. S. Hlaing, M. M. Aung, M. T. Nwe, I. Lamraoui and Y. Yan, *Int. J. Mol. Sci.*, 2020, **21**, 3588.

10 R. Frankowski, A. Zgoła-Grześkowiak, W. Smułek and T. Grześkowiak, *Appl. Biochem. Biotechnol.*, 2020, **191**, 1100–1110.

11 Y. Huang, Q. Li, Z. Guan, D. Xia and Z. Wu, *J. Water Process Eng.*, 2023, **52**, 103564.

12 S. Wang, Q. Wu, B. Yan, Y. Guo, W. Xia, J. Li, F. Cui and J. Tian, *Sep. Purif. Technol.*, 2022, **291**, 120874.

13 M. A. Martín-Lara, M. Calero, A. Ronda, I. Iáñez-Rodríguez and C. Escudero, *Water*, 2020, **12**, 2150.

14 N. U. M. Nizam, M. M. Hanafiah, E. Mahmoudi, A. A. Halim and A. W. Mohammad, *Sci. Rep.*, 2021, **11**, 8623.

15 H. Sayğılı, F. Güzel and Y. Önal, *J. Cleaner Prod.*, 2015, **93**, 84–93.

16 C. Djilani, R. Zaghdoudi, F. Djazi, B. Bouchekima, A. Lallam, A. Modarressi and M. Rogalski, *J. Taiwan Inst. Chem. Eng.*, 2015, **53**, 112–121.

17 I. Chaari, E. Fakhfakh, M. Medhioub and F. Jamoussi, *J. Mol. Struct.*, 2019, **1179**, 672–677.

18 R. Pleșa Chicinaș, H. Bedelean, R. Stefan and A. Măicăneanu, *J. Mol. Struct.*, 2018, **1154**, 187–195.

19 D. Fu, Q. Zhang, P. Chen, X. Zheng, J. Hao, P. Mo, H. Liu, G. Liu and W. Lv, *RSC Adv.*, 2021, **11**, 18308–18320.

20 A. Elaouni, M. E. Ouardi, M. Zbair, A. BaQais, M. Saadi and H. A. Ahsaine, *RSC Adv.*, 2022, **12**, 31801–31817.

21 J. Li, X. Wang, G. Zhao, C. Chen, Z. Chai, A. Alsaedi, T. Hayat and X. Wang, *Chem. Soc. Rev.*, 2018, **47**, 2322–2356.

22 L. Jiao, J. Y. R. Seow, W. S. Skinner, Z. U. Wang and H.-L. Jiang, *Mater. Today*, 2019, **27**, 43–68.

23 P. N. Dave and A. Gor, in *Handbook of Nanomaterials for Industrial Applications*, ed. C. Mustansar Hussain, Elsevier, 2018, pp. 36–66.

24 M. E. Davis and M. E. Brewster, *Nat. Rev. Drug Discovery*, 2004, **3**, 1023–1035.

25 T. Loftsson and H. Friðriksdóttir, *Int. J. Pharm.*, 1998, **163**, 115–121.

26 G. Xu, X. Xie, L. Qin, X. Hu, D. Zhang, J. Xu, D. Li, X. Ji, Y. Huang, Y. Tu, L. Jiang and D. Wei, *Green Chem.*, 2019, **21**, 6062–6072.

27 T. Gong, Y. Zhou, L. Sun, W. Liang, J. Yang, S. Shuang and C. Dong, *RSC Adv.*, 2016, **6**, 80955–80963.

28 C. Yang, H. Huang, T. Ji, K. Zhang, L. Yuan, C. Zhou, K. Tang, J. Yi and X. Chen, *Polym. Int.*, 2019, **68**, 805–811.

29 K. V. Ragavan and N. K. Rastogi, *Carbohydr. Polym.*, 2017, **168**, 129–137.

30 J. H. Lee and S.-Y. Kwak, *J. Appl. Polym. Sci.*, 2020, **137**, 48475.

31 S. R. Patel and M. P. Patel, *Polym. Bull.*, 2022, **79**, 11079–11101.

32 S. R. Patel, R. H. Patel and M. P. Patel, *J. Macromol. Sci., Part A*, 2021, **58**, 97–110.

33 P. N. Dave, B. Kamaliya, P. M. Macwan and J. H. Trivedi, *Curr. Res. Green Sustainable Chem.*, 2023, 6, 100349.

34 P. N. Dave, L. V. Chopda and B. P. Kamaliya, *Chem. Eng. Technol.*, 2023, 46, 997–1004.

35 R. Ramadan and A. M. Ismail, *J. Inorg. Organomet. Polym. Mater.*, 2022, 32, 984–998.

36 R. Sirach and P. N. Dave, *J. Hazard. Mater. Adv.*, 2023, 10, 100300.

37 M. A. Medeleanu, D. I. Hădărugă, C. V. Muntean, G. Popescu, M. Rada, A. Hegheș, S. E. Zippenfening, C. A. Lucan (Banciu), A. B. Velciov, G. N. Bandur, N. G. Hădărugă and M. Riviș, *Carbohydr. Polym.*, 2021, 265, 118079.

38 G. G. Hacıosmanoğlu, T. Doğruel, S. Genç, E. T. Oner and Z. S. Can, *J. Hazard. Mater.*, 2019, 374, 43–49.

39 K. Rekos, Z.-C. Kampouraki, C. Sarafidis, V. Samanidou and E. Deliyanni, *Materials*, 2019, 12, 1987.

40 L. D. Quan, N. H. Dang, T. H. Tu, V. N. Phuong Linh, L. T. Mong Thy, H. M. Nam, M. T. Phong and N. H. Hieu, *Synth. Met.*, 2019, 255, 116106.

41 M. Mondal, S. Basak, S. Ali, D. Roy, M. S. Haydar, K. Sarkar, N. N. Ghosh, K. Roy and M. N. Roy, *Environ. Sci. Pollut. Res.*, 2023, 30, 43300–43319.

42 A. Z. M. Badruddoza, A. S. H. Tay, P. Y. Tan, K. Hidajat and M. S. Uddin, *J. Hazard. Mater.*, 2011, 185, 1177–1186.

43 G. Leofanti, M. Padovan, G. Tozzola and B. Venturelli, *Catal. Today*, 1998, 41, 207–219.

44 Y. Li, P. Lu, J. Cheng, X. Zhu, W. Guo, L. Liu, Q. Wang, C. He and S. Liu, *Talanta*, 2018, 187, 207–215.

45 L. Ai, J. Hu, X. Ji and H. Zhao, *RSC Adv.*, 2019, 9, 26224–26229.

46 M. Kotronia, E. Kavetsou, S. Loupassaki, S. Kikionis, S. Vouyiouka and A. Detsi, *Bioengineering*, 2017, 4, 74.

47 S. M. R. Paran, H. Vahabi, M. Jouyandeh, F. Ducos, K. Formela and M. R. Saeb, *J. Appl. Polym. Sci.*, 2019, 136, 47483.

48 L. Joseph, Q. Zaib, I. A. Khan, N. D. Berge, Y.-G. Park, N. B. Saleh and Y. Yoon, *Water Res.*, 2011, 45, 4056–4068.

49 M. H. Dehghani, A. H. Mahvi, N. Rastkari, R. Saeedi, S. Nazmara and E. Iravani, *Desalin. Water Treat.*, 2015, 54, 84–92.

50 R. V. P. Antero, A. C. F. Alves, P. de T. Ferreira Sales, S. B. de Oliveira, S. A. Ojala and S. S. Brum, *Chem. Eng. Commun.*, 2019, 206, 1498–1514.

51 S. Rovani, J. J. Santos, S. N. Guilhen, P. Corio and D. A. Fungaro, *RSC Adv.*, 2020, 10, 27706–27712.

52 J. Peng, Y. Li, X. Sun, C. Huang, J. Jin, J. Wang and J. Chen, *ACS Appl. Mater. Interfaces*, 2019, 11, 4328–4337.

53 W. Xin, X. Li and Y. Song, *J. Chem. Technol. Biotechnol.*, 2020, 95, 1666–1674.

54 B. Mahanty, S. K. Behera and N. K. Sahoo, *Sep. Sci. Technol.*, 2023, 58, 1275–1282.

55 C. V. Floare-Avram, O. Marincas, I. Feher, F.-D. Covaciu, C. G. Floare, M. D. Lazar and D. A. Magdas, *Anal. Lett.*, 2023, 56, 272–285.

56 C. Mo, M. Faheem, S. Aziz, S. Jian, W. Xue, T. Yuyang, D. Shuang and Z. Guangshan, *RSC Adv.*, 2020, 10, 26335–26341.

57 S. Mantovani, T. Dorina Marforio, S. Khaliha, A. Pintus, A. Kovtun, F. Tunioli, L. Favaretto, A. Bianchi, M. Luisa Navacchia, V. Palermo, M. Calvaresi and M. Melucci, *Environ. Sci.: Water Res. Technol.*, 2023, 9, 1030–1040.

58 T. Ahamad, M. Naushad, A. N. Alhabarah and S. M. Alshehri, *Int. J. Biol. Macromol.*, 2019, 132, 1031–1038.

59 A. Supong, P. C. Bhomick, M. Baruah, C. Pongener, U. B. Sinha and D. Sinha, *Sustainable Chem. Pharm.*, 2019, 13, 100159.

60 P. Wang, X. Zhou, Y. Zhang, L. Wang, K. Zhi and Y. Jiang, *RSC Adv.*, 2016, 6, 102348–102358.